

**G. Pullan<sup>1</sup>**

Visiting Associate Professor  
Gas Turbine Laboratory,  
Massachusetts Institute of Technology,  
77 Massachusetts Avenue,  
Cambridge, MA 02139

**A. M. Young**

Whittle Laboratory,  
University of Cambridge,  
1 JJ Thomson Avenue,  
Cambridge CB3 0DY, UK

**I. J. Day**

Whittle Laboratory,  
University of Cambridge,  
1 JJ Thomson Avenue,  
Cambridge CB3 0DY, UK

**E. M. Greitzer**

Gas Turbine Laboratory,  
Massachusetts Institute of Technology,  
77 Massachusetts Avenue,  
Cambridge, MA 02139

**Z. S. Spakovszky**

Gas Turbine Laboratory,  
Massachusetts Institute of Technology,  
77 Massachusetts Avenue,  
Cambridge, MA 02139

# Origins and Structure of Spike-Type Rotating Stall

*In this paper, we describe the structures that produce a spike-type route to rotating stall and explain the physical mechanism for their formation. The descriptions and explanations are based on numerical simulations, complemented and corroborated by experiments. It is found that spikes are caused by a separation at the leading edge due to high incidence. The separation gives rise to shedding of vorticity from the leading edge and the consequent formation of vortices that span between the suction surface and the casing. As seen in the rotor frame of reference, near the casing the vortex convects toward the pressure surface of the adjacent blade. The approach of the vortex to the adjacent blade triggers a separation on that blade so the structure propagates. The above sequence of events constitutes a spike. The computed structure of the spike is shown to be consistent with rotor leading edge pressure measurements from the casing of several compressors: the centre of the vortex is responsible for a pressure drop and the partially blocked passages associated with leading edge separations produce a pressure rise. The simulations show leading edge separation and shed vortices over a range of tip clearances including zero. The implication, in accord with recent experimental findings, is that they are not part of the tip clearance vortex. Although the computations always show high incidence to be the cause of the spike, the conditions that give rise to this incidence (e.g., blockage from a corner separation or the tip leakage jet from the adjacent blade) do depend on the details of the compressor. [DOI: 10.1115/1.4028494]*

## Introduction

It has been known for more than a decade that there are two distinct routes to compressor rotating stall with different onset criteria for each [1]. One is through the growth of small amplitude (compared to the mean velocity) disturbances with length scale of the compressor circumference. The initial stages of this process are in accord with the linear-to-nonlinear wave evolution described by established theories of compressor instability [2]. A second route, however, is through transient disturbances with much shorter length scale (several blade pitches), which, as detected by probes upstream of a blade row, are of large amplitude compared to the mean velocity and are not described by existing analyses. The disturbances in this second route have been called “spikes,” in reference to the sharp waveform they exhibit compared to the first type of disturbance. The phenomena responsible for the formation of spikes are not well understood.

In this paper, we define the fluid dynamic processes responsible for the occurrence and formation of spikes as a route to compressor rotating stall. It will be shown that the spike is linked to separation from the leading edge in the tip region. Further, spike stall has been found in axial compressors with tip clearance, axial compressors with tip shrouds (hence, no tip clearance or relatively rotating endwall), and in centrifugal compressor vaned diffusers. The implication we draw from these experimental results, and from the simulations, is that the proposed mechanism appears generic and applicable to a broad range of turbocompressors.

We emphasize the generic aspects in what follows, although there is an important caveat in that the circumstances that promote

the leading edge separation in a specific situation do depend on the details of the turbomachinery. In this context, a rough analogy can be made with the first route to instability. It is well-known that the conditions under which long length scale, small amplitude, disturbances grow into rotating stall are associated with operation on a positively sloped compressor pressure rise characteristic; that is the generic finding concerning long length scale disturbances. There are, however, multiple fluid dynamic processes by which this criterion can be achieved: increased blade loss, increased tip clearance flow blockage, increased deviation, or a combination of two or more of these, which occurs depending on design specifics, and any or all can lead to a situation in which the pressure rise characteristic peaks. We will show that an analogous set of circumstances is present in the description of spike stall, in that there are many possible causes for the increase in incidence required to trigger a leading edge separation.

The organization and scope of the paper is as follows. We first show experimental measurements from axial compressors with tip clearance and with a shrouded tip, and from a centrifugal compressor with vaned diffuser, as examples of spike stall. Following that we introduce the proposed vortex behavior and the structure of the spike to address, in qualitative terms, the question of “what is a spike?” A series of unsteady simulations of the NASA E<sup>3</sup> Rotor B are interrogated to provide insight into the quantitative nature of spike stall, with the understanding gained then applied to interpret further computations and detailed experimental information from an additional compressor.

## Experimental Information on Spike Stall

Spike-type rotating stall inception is known to occur in axial flow compressors near the tip of the rotor blade leading edge. The stall onset is apparent in time-resolved casing static pressure measurements from probes at different circumferential locations

<sup>1</sup>Present address: Whittle Laboratory, University of Cambridge, 1 JJ Thomson Avenue, Cambridge CB3 0DY, UK.

Contributed by the International Gas Turbine Institute (IGTI) of ASME for publication in the JOURNAL OF TURBOMACHINERY. Manuscript received August 9, 2014; final manuscript received August 11, 2014; published online November 18, 2014. Editor: Ronald Bunker.

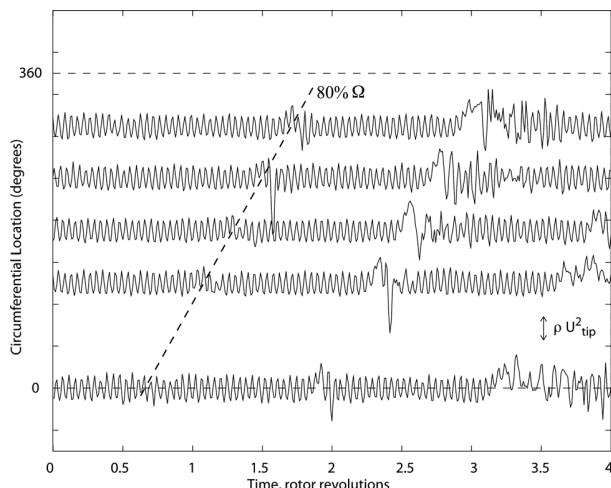


**Fig. 1 Spike stall inception in MHI single-stage axial compressor with rotor tip clearance of 1% span. (Data courtesy of Takasago R&D Center, MHI.)**

upstream of a rotor. Figure 1 is an example, which shows data from five pressure transducers in an MHI single-stage axial compressor with hub-to-tip ratio of 0.7 and rotor blade tip clearance of 1% span. The spike disrupts the blade passing waveforms by a sudden rise in pressure, followed by a rapid pressure drop. Similar traces have been reported in Refs. [3–5] and elsewhere. The pattern grows in amplitude and length scale as it travels around the circumference at approximately 80% of rotor speed before evolving into rotating stall.

Although it has been conjectured that tip clearance flow is necessary for spike formation, there are at least two sets of experiments that show this not to be the case, the first on a tip shrouded axial compressor and the second on a centrifugal compressor with vaned diffuser. In the first of these, a single-stage axial compressor at MIT was run with a sheet metal shroud to prevent tip leakage [6] and data were taken on the type of stall onset. Figure 2 shows the resulting time-resolved casing static pressures during throttle ramps into stall. Stall inception in the shrouded compressor is seen to consist of spike-like disturbances that rotate around the annulus at about 70% of rotor speed and evolve into a full-span stall cell.

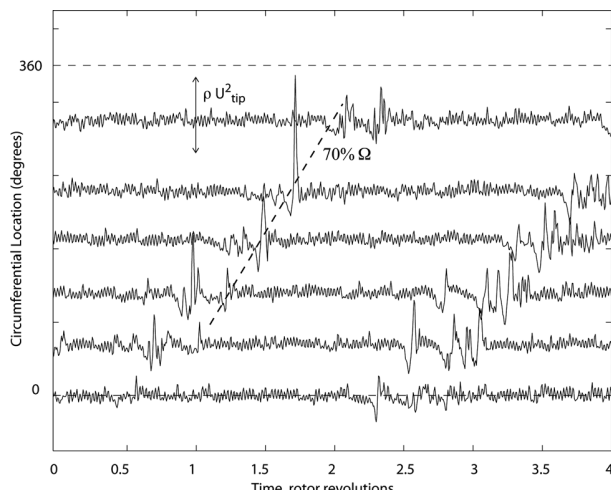


**Fig. 2 Spike stall inception in the MIT single-stage axial compressor with tip shrouded rotor [6]**

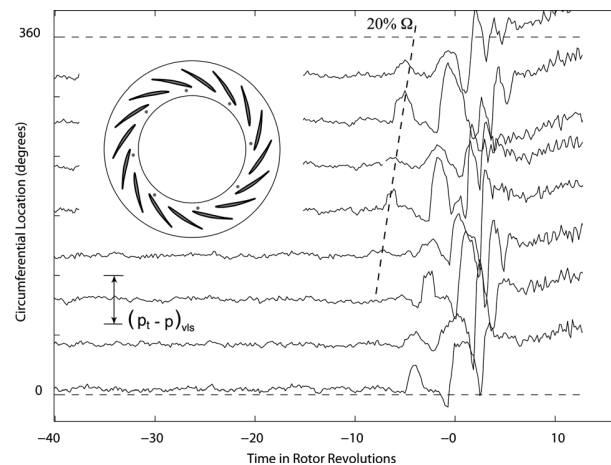


**Fig. 3 Spike stall inception in the vaned diffuser of a centrifugal compressor [7]**

In the second set of experiments, measurements carried out in a centrifugal compressor vaned diffuser suggest that spike-type stall precursors occur near the leading edge of shrouded diffuser vanes [7]. In this case, the precursors are larger in spatial extent and slower in rotation rate than in axial machines, consistent with the larger blade pitch. Figure 3 shows the time-resolved shroud static pressures, at eight locations around the circumference, at a radial station between the impeller and the diffuser. The disturbance propagates at about 20% of rotor speed.<sup>2</sup> The sudden rise in pressure followed by the rapid pressure drop can again be seen. Unsteady calculations reveal that flow separation at the diffuser leading edge, caused by high incidence near the shroud, leads to reversed radial flow, allowing vorticity shed from the leading edge to move inward and recirculate around the circumference. As blockage accumulates, the spikes grow, leading to flow breakdown into rotating stall [8].

In support of the comments in the Introduction, therefore, the inference we draw is that spike-like prestall patterns occur in centrifugal as well as axial turbomachinery and that blade tip leakage flow is not a necessary condition for their formation.

### A Conceptual Picture of Spike Flow Structure

While the above two sections give information on the flows in which spikes form, and while there are descriptions of the conditions that accompany this formation [1,4,9], our perspective is that there exists no description of the fluid dynamic events which are causally linked with the creation of the spike. Providing this link, based on interrogations of numerical simulations and experimental measurements, is the main contribution of this paper.

Most of the calculation results to be presented are instantaneous snapshots of pressure and radial vorticity near the compressor casing. Anticipating those results, we state that they allow a conceptual picture to be built up of the key features of the vortical spike structure as depicted in Fig. 4: (i) High incidence results in a separation from the leading edge in the outer part of the blade. (ii) The vorticity shed by this separation forms a vortex tube that spans from blade to casing as was suggested by Inoue et al. [10]. (iii) The upper “end” of the vortex<sup>3</sup> is on the casing and the lower end is on the blade. The convection of the vortex, as seen in the rotor

<sup>2</sup>This speed is measured in the same (absolute) frame of reference as the stalling blade row. For stall inception occurring in a rotor, a spike travelling at 80% of wheel speed in the absolute frame has a speed of 20% in the relative frame.

<sup>3</sup>Vortex lines cannot end in a fluid, and what we have drawn is a section of a vortex tube. The vortex lines within the tube continue in thin layers on the casing and on the rotor (at these surfaces they must be tangential to the surface) rather than in the form of a discrete vortex. For simplicity, we have not drawn the vortex lines outside of the section of the tube that is shown.

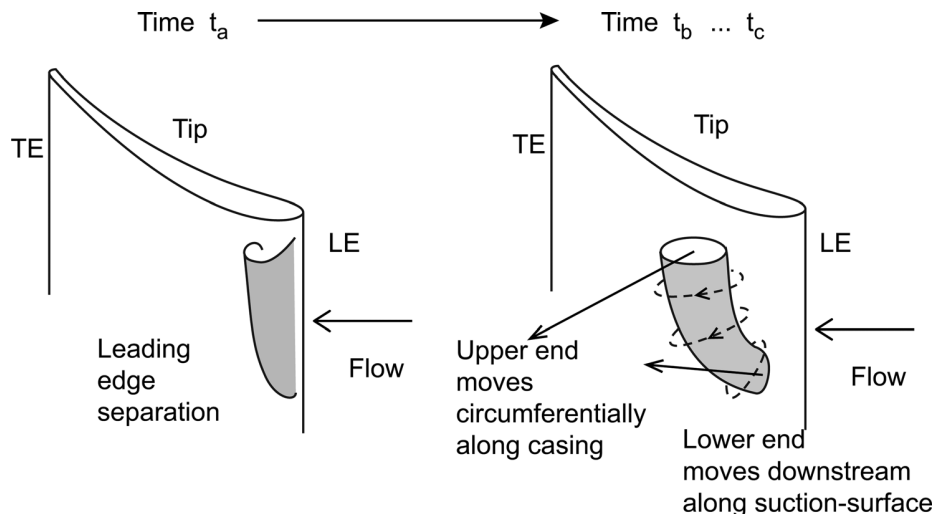


Fig. 4 The vortical structure and propagation of the spike

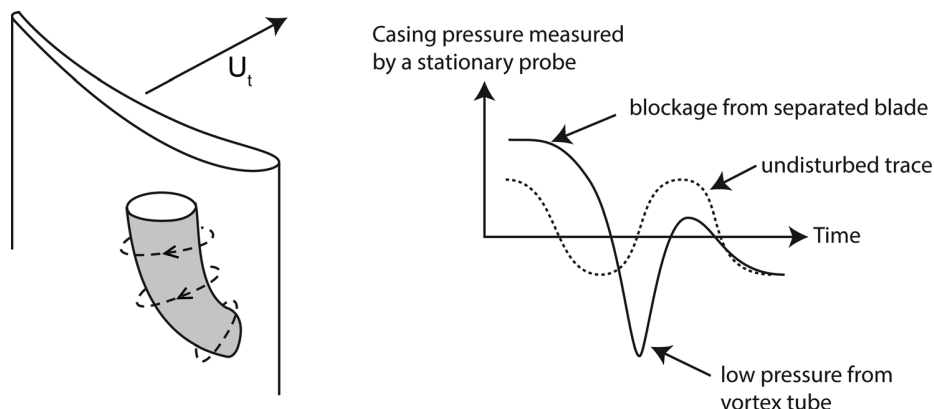


Fig. 5 The connection between spike structure and casing pressure trace

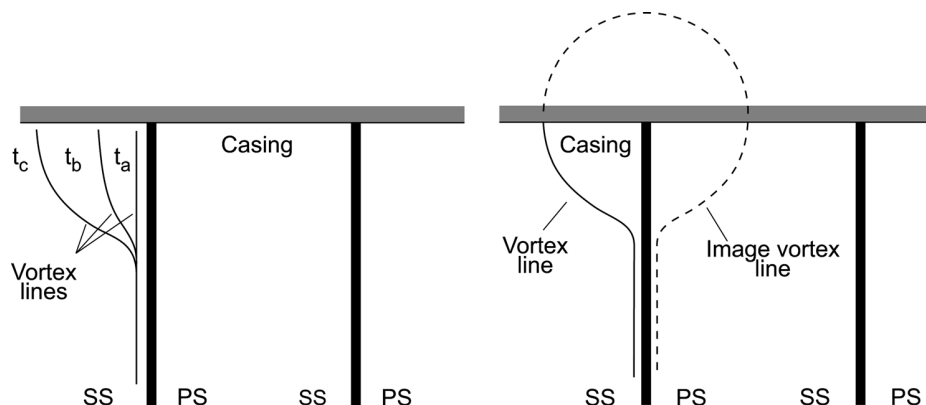


Fig. 6 Vortex filament evolution from leading edge separation (left), and image system showing vortex ring (right). View is upstream along stagger angle.

frame of reference, is indicated by the arrows. (iv) A new separation then forms on the next blade and the spike propagates. Simulations both with and without clearance show this structure, and we thus infer that the formation of, and vorticity source for, the vortex shed from the leading edge is not associated with the tip clearance vortex.

A pressure transducer just upstream of the leading edge at the casing will respond to the proposed spike structure in the manner

shown in Fig. 5. The stationary sensor first encounters the potential field of the blockage caused by the leading edge separation (a pressure rise) then a sharp pressure drop as the vortex tube crosses the transducer. The resultant up-down waveform is a characteristic of a spike.

Figure 6 is a sketch of the time evolution of the "vortex skeleton" associated with this behavior. It shows vortex filaments near the blade leading edge region, looking upstream, roughly along

**Table 1 Design parameters for the E<sup>3</sup> Rotor B compressor**

Design flow coefficient $V_x/U_t$	0.41
Design stage pressure rise coefficient $\Delta p_0/0.5\rho U_t^2$	0.56
Hub to tip radius ratio $r_h/r_t$	0.85
Tip diameter	1524 mm
Number of rotor blades	54
Rotational speed	722 rpm

the blade stagger angle. The blades are drawn as heavy vertical lines. The sketch on the left side of Fig. 6 shows the passage at three time instants.<sup>4</sup> At time  $t_a$ , there is no separation, and the vortex filaments are close to the suction surface. At time  $t_b$ , the upper part of the filament (and the surrounding vortex tube) has detached from the suction side, and at time  $t_c$  the upper part has moved further away from the suction surface. In terms of image vorticity, as in the right side sketch of Fig. 6, the configuration at time  $t_c$  appears as a vortex ring, with sense of vorticity implying upstream propagation, given an appropriate combination of low enough onset velocity and strong enough circulation.

The conceptual picture of the spike that we put forward appears to apply to the different geometries examined; axial compressors with tip clearance, tip shrouded axial compressors, and centrifugal compressors. It is also consistent with the simulations, with the experimental findings both overall (the view of spikes as an incidence-related phenomenon localized to the tip region), and detailed (the characteristic wave form of pressure transducers upstream of the leading edge, and the casing static pressure field measured by arrays of transducers).

### Summary of the Computational Approach

Information on the computational method is provided in the Appendix and only a brief summary is given here. The computations were performed using Turbostream [11], a structured multi-block URANS code based on the algorithms developed by Denton [12]. A single equation Spalart–Allmaras turbulence model was used. All computations were performed on graphics processing units (GPU), allowing an order of magnitude reduction in runtime compared to running the same calculations on conventional processors.

### E<sup>3</sup> Rotor B Simulations

**Introduction.** The NASA E<sup>3</sup> Rotor B is used to investigate the fluid structures at spike onset. This rotor is chosen because it has been the subject of a previous study of spike-type stall inception [9], the information on the geometry is public, and it is representative of a range of machines of technological interest. The rotor is characterized by the parameters listed in Table 1 and detailed information is provided in Ref. [13].

The computations are presented in order of increasing complexity: a linear cascade of translating E<sup>3</sup> Rotor B tip profiles; E<sup>3</sup> Rotor B without tip clearance; and E<sup>3</sup> Rotor B with tip clearance. This progression has two advantages. First, it allows the details of the spike to be diagnosed first in situations with fewer interacting phenomena than when tip clearance is present and, second, it facilitates the identification of mechanisms common to all cases.

Figure 7 shows computed total-to-static characteristics for the three E<sup>3</sup> Rotor B geometries. The circles denote unsteady single passage computations, and the squares denote computations carried out using a domain of a quarter of the circumference (for blade periodicity, 93 deg). Only stable operating points are indicated. Two observations can be made. First, in each case, the characteristic has a negative slope at the stall point and we therefore expect the simulations to take the spike route to rotating stall.

<sup>4</sup>These times correspond to the computations in Figs. 14(a), 14(b), and 14(c), as will be described.

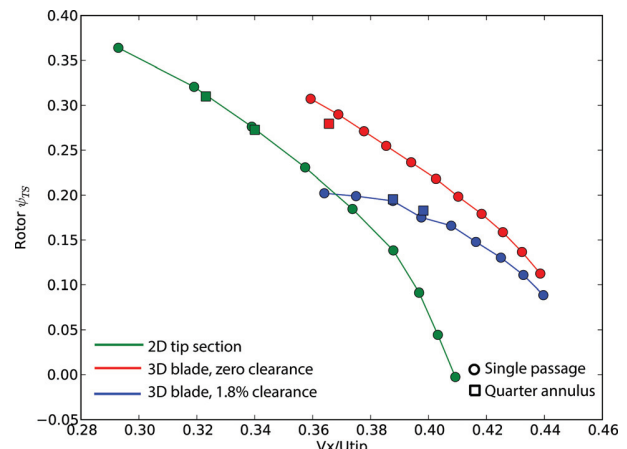


**Fig. 7 Computed total-to-static characteristics for the E<sup>3</sup> Rotor B**

Second, the quarter-sector calculations stall at a higher flow coefficient than the single passage computations. This implies that a sufficient number of passages must be modeled in order to resolve the early stages of spike stall inception. The pressure rise associated with the initial spike is approximately two or three pitches in circumferential extent and at least double this number of passages are likely to be required to resolve the formation of a spike.

**Two-Dimensional Tip Section Computations.** Based on the evidence that tip clearance is not required for spike formation, the first set of simulations we explore are for a two-dimensional linear cascade of E<sup>3</sup> tip section profiles. Following the procedure described in the Appendix, an unsteady calculation of a single passage domain was used to identify the stability limit. Then, a “full wheel” (periodic over 54 passages) domain was used, with the flow coefficient gradually reduced until stall onset. To initiate stall at a known location for detailed analysis, four adjacent blades were restaggered (permanently) by 1 deg to increase their incidence.

Figure 8 shows a set of computed nondimensional static pressure traces at six equispaced locations across the 54 passages, 10% of axial chord upstream of the leading edge. A perturbation in the upstream potential field of the blades is first detected, at the restaggered blades, at time  $t_1$ . Within half a rotor revolution, this disturbance has grown and the pressure trace now shows the characteristic up-down waveform of a spike.

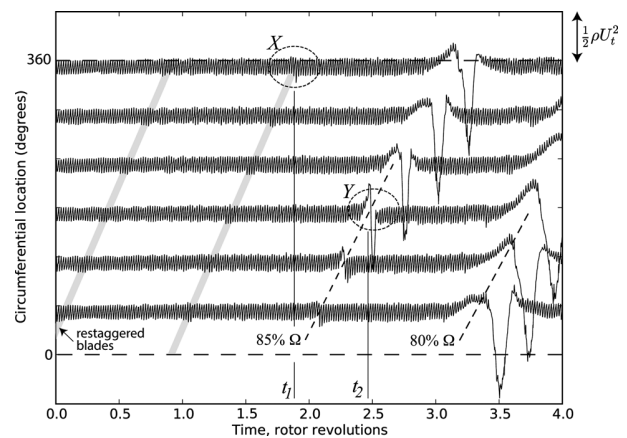


**Fig. 8 Spike stall inception in 2D E<sup>3</sup> tip profile cascade computation**

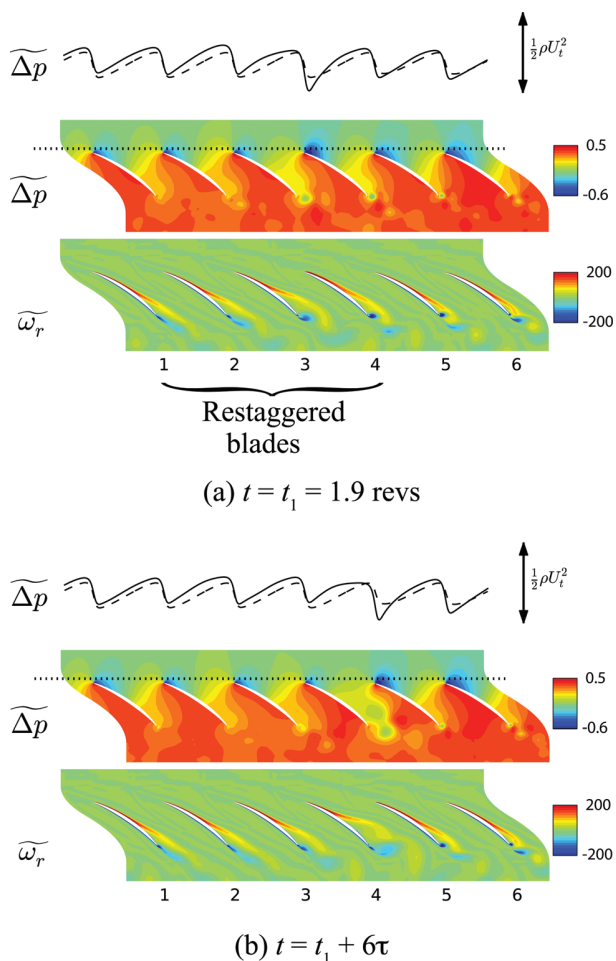


**Fig. 9** Blade loading perturbation caused by suction-surface separation in 2D  $E^3$  tip profile cascade

The flow field accompanying the initial disturbance (time  $t_1$ , location "X") and spike (time  $t_2$ , location "Y") are now examined to determine the origins, structure, and propagation mechanism of the spike. Figure 9 is representative of a type of plot that will be used frequently during the paper. The solid and dashed line traces at the top of the figure show the static pressure at 10% of axial chord upstream of the leading edge (at the location indicated by the dotted line). The solid line is the instantaneous trace; the dashed line is the time-averaged trace (averaged in the relative frame over one rotor revolution immediately prior to stall inception). A line representing  $0.5\rho U_t^2$  is drawn on the right of the plot to provide a scale. Below these traces are contour plots of nondimensional static pressure coefficient,  $\Delta\tilde{p}$ , and radial component of vorticity,  $\tilde{\omega}_r$ . Each blade is assigned a number shown at the bottom of the figure and time is indicated with reference to the accompanying pressure trace plot (Fig. 8) with  $\tau$  indicating the blade passing period.

Figure 9 shows the flow field associated with the initial disturbance at two time instants. The pressure trace deviates from the time-averaged value due to a perturbation in leading edge loading. In Fig. 9(a), the suction-surface boundary layers of blades 1–3 are separated at approximately midchord; the consequent blockage means that the pressure upstream of the blades rises. The separation on blade 3 causes an increase in incidence on to blade 4; the resultant increase in leading edge loading causes a local drop in the upstream pressure trace. The suction-surface boundary layer of blade 4 cannot sustain the required deceleration and separates, increasing the incidence on to blade 5, Fig. 9(b). In this way, the

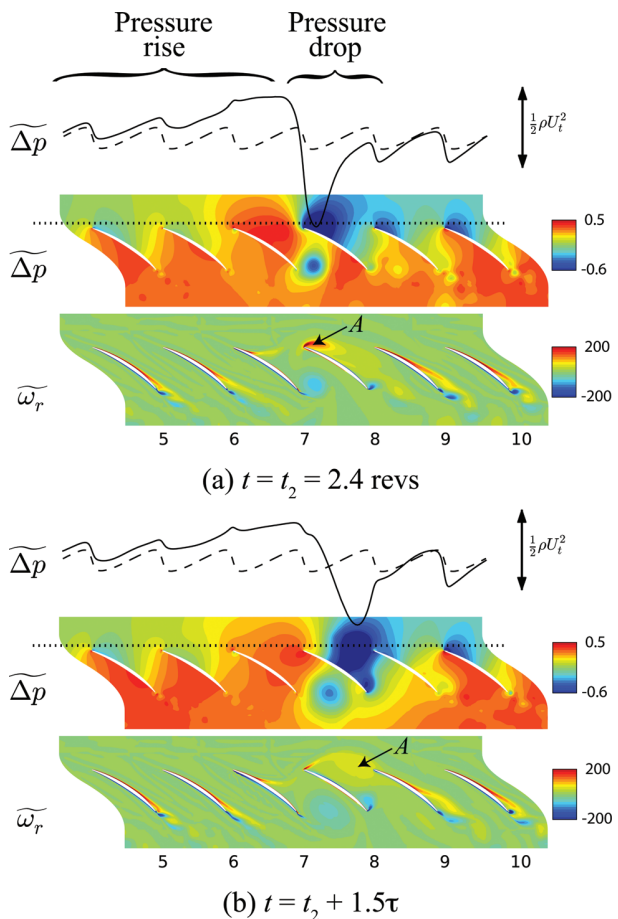


**Fig. 10** Spike caused by leading edge separation in 2D  $E^3$  tip profile cascade

disturbance has propagated, by one blade pitch, in the way proposed by Emmons et al. [14].

The suction surface separations continue to propagate from blade to blade, moving away from the restaggered blades where they first occurred. The separations move further forward with each blade because of the following positive feedback mechanism: blockage from the separation on one blade increases the incidence on to the next, causing the next blade to separate closer to the leading edge and hence create a larger blockage, and so on. At the time shown in Fig. 10(a), the separation occurs close to the leading edge of blade 7 and at the leading edge of blade 8. The passage between blades 7 and 8 is almost completely blocked (causing the *pressure rise* on the upstream trace). The vorticity that is shed by the leading edge of blade 8 rolls up into a vortex (labeled "A") that convects toward the leading edge of blade 9 in Fig. 10(b)—the low pressure associated with this vortex is responsible for the sharp *pressure drop* seen on the upstream trace. Once it arrives at blade 9, vortex "A" triggers a new leading edge separation, causing a new shedding of vorticity. The propagation of the spike therefore includes the convection of shed vorticity from one blade to the next. In the relative frame, this means that the pressure drop (the low pressure zone associated with the shed vortex) leads the pressure rise (high pressure caused by the blocked passages). In the absolute frame, stationary pressure probes measure a positive pulse followed by a negative pulse, see Fig. 5.

The two-dimensional calculations thus show that leading edge separation is responsible for the spike. The spike propagates by the convection of the vortex that is shed from the leading edge. This will be shown to be the case in all the configurations presented in the paper. For this two-dimensional geometry, the high

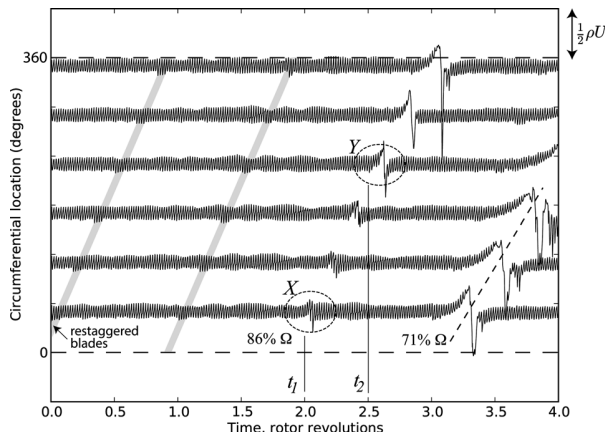


**Fig. 11 Spike stall inception in  $E^3$  rotor computation, zero clearance**

incidence responsible for the leading edge separation was caused by blockage from separated blade surface boundary layers.

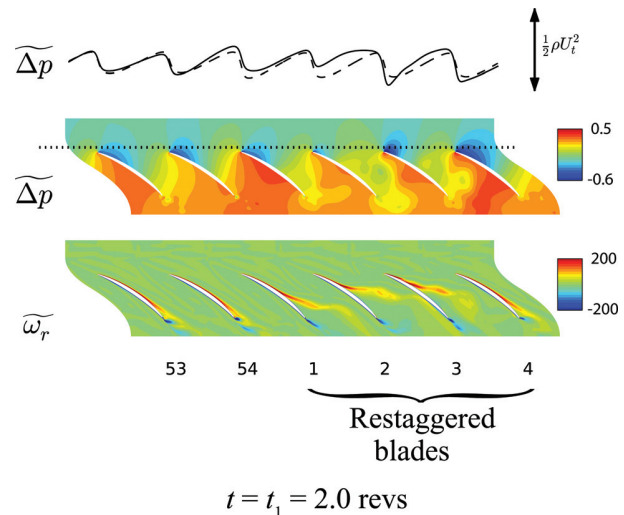
**Computations of 3D Blade With Zero Tip Clearance.** We extend the preceding two-dimensional description to three dimensions and examine the full  $E^3$  Rotor B blade. The first set of three-dimensional calculations to be shown is with zero tip clearance. While the setup is artificial because the casing is stationary (rather than rotating as in a shrouded rotor), it is a limiting case for the unshrouded rotor, providing a step upward in complexity toward the full situation. A similar procedure to that followed for the two-dimensional computations was adopted: single passage unsteady simulations ( $1.4 \times 10^6$  nodes, 12 operating points) to obtain an approximate stability limit; quarter annulus (14 blades, 93 deg) simulations ( $19 \times 10^6$  nodes, 2 operating points) with four restaggered blades to obtain the operating point at spike onset; full annulus ( $74 \times 10^6$  nodes, 2 operating points) simulations to be certain that the spike development and propagation is unaffected by the imposition of a 4-per-rev repeating sector of 1 deg increased incidence.

Figure 11 shows simulated time traces from six static pressure probes arranged around the casing circumference at 10% of axial chord upstream of the rotor leading edge. The similarities between this plot and that of the two-dimensional linear cascade of tip section profiles (Fig. 8) can be seen. The initial perturbation to the regular upstream potential field of the blades is seen at  $t_1$ . Within half of a rotor revolution, this disturbance has formed a spike (time  $t_2$ , location "Y").

In the same manner as the two-dimensional case, the perturbation to the blade loadings in zone "X" of Fig. 11 is caused by separation from the blade suction surface that occurs first on the restaggered blades, Fig. 12. In common with all similar plots from three-dimensional simulations shown in this paper, the flow field and pressure traces in Fig. 12 are from a cut at 95% span so the separation shown is actually a slice through a three-dimensional corner separation. Blockage from the corner separations on blades 1 and 2 causes the pressure rise in the upstream trace. The high incidence on blade 3 results in high leading edge loading and a small pressure drop in the trace.

The first separation from the leading edge of a blade is seen in Fig. 13(a) and occurs at blade 6. The shed vorticity rolls up into vortex "B" that convects toward, and in front of, the leading edge of blade 7. Here, as was the case in the two-dimensional simulations, the vortex triggers a new leading edge separation (from blade 7) and vorticity will be shed.

The key difference, as regards the spike structure, between the two-dimensional cascade and the full blade row is the spanwise extent of the leading edge separation. To illustrate this, a sequence



**Fig. 12 Blade loading perturbation caused by growth of corner separation in  $E^3$  rotor, zero clearance, 95% span**

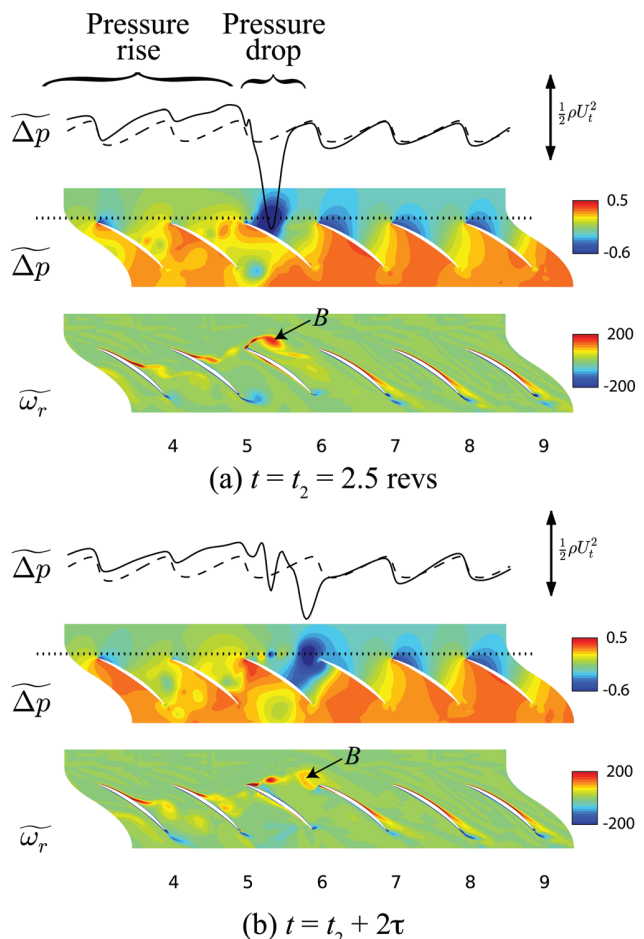
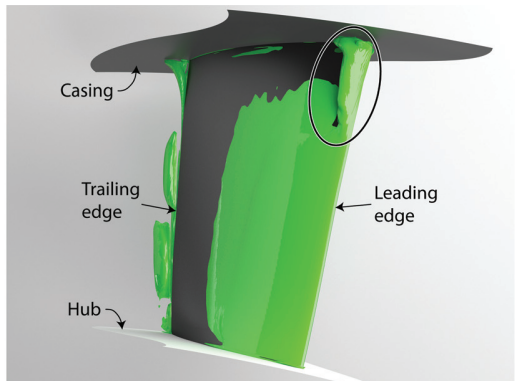


**Fig. 13 Spike caused by leading edge separation in  $E^3$  rotor, zero clearance, 95% span**

of snapshots of blade 6 showing an isosurface of the  $\lambda_2$  vortex criterion [15] is presented in Fig. 14. The  $\lambda_2$  isosurface can be regarded as a marker for vorticity associated with discrete swirling flow structures (i.e., vortices) rather than vorticity in a sheet or shear layer (a boundary layer, for example). Thus, even though



(a)  $t = t_2 - \tau$ ; leading edge separation circled



(b)  $t = t_2 - 0.5\tau$ ; vortex tube forms, upper end moves circumferentially along casing



(c)  $t = t_2$ ; lower end of tube moves downstream along suction-surface

**Fig. 14 Structure of the spike. Isosurface of the  $\lambda_2$  vortex criterion, E<sup>3</sup> rotor zero clearance.**

vortex lines cannot end in a fluid, the  $\lambda_2$  surfaces can do so. The final snapshot in the series of three, Fig. 14(c), is at the same time instant as Fig. 13(a); two preceding time instances are also shown so that the development of the structure can be observed.

Figure 14(a) shows that the spanwise nonuniform incidence, greatest at the tip, has caused a leading edge separation (circled in the figure) to form over the outer 25% of span of blade 6. In Fig. 14(b), the vorticity shed from the blade by this separation has formed a vortex-tube. The vortex tube appears to terminate at the casing and at the suction-surface because the vortex filaments become tangential to the solid surfaces in a layer and are thus not indicated by the  $\lambda_2$  criterion. The rotation of the vortex tube is

indicated by the dashed arrows, and the convection of the casing end of the tube in the circumferential direction toward the pressure-side of the adjacent blade is also shown. Finally, in Fig. 14(c), the suction-surface end of the tube is seen to be moving in a streamwise direction toward the trailing edge of the blade.

The motion of the vortex tube is therefore summarized as follows. The end of the tube at the casing moves circumferentially toward the leading edge of blade 7, where it triggers a new leading edge separation; the end on the suction-surface of blade 6 proceeds downstream toward the trailing edge. This is evidence for the structure shown in Figs. 4 and 6. We note again the resemblance of this structure to that proposed by Inoue et al. [10,16–18] and, more recently, by Yamada et al. [19].

The calculations of the E<sup>3</sup> Rotor B with zero clearance show the same mechanisms for the formation of the spike and its propagation as in the two-dimensional simulations. The spike is created by a leading edge separation over the outer 25% of span that causes vorticity to be shed. The resulting vortex tube has one end at the casing—this convects to the leading edge of the next blade in the same way as the vortex in the two-dimensional simulations—and one on the suction surface which travels downstream. For this three-dimensional, zero clearance, geometry, the high incidence responsible for the leading edge separation was caused by blockage from a corner separation.

**Computations of 3D Blade With Tip Clearance.** The final set of computations of the E<sup>3</sup> Rotor B was performed with a tip clearance of 1.8% of chord. The computational procedure and run times for this set of simulations were similar to those described above for the zero clearance case.

*Approaching Stall.* As the E<sup>3</sup> rotor is throttled toward stall, the interface line that demarcates the oncoming flow from the over-tip leakage flow rotates toward the circumferential direction until, just before stall, it is almost coincident with the leading edge plane. This is illustrated by the time-averaged entropy contours, at 95% span, shown in Fig. 15. The operating point shown is stable.

It is also found that the tip clearance flow is highly unsteady, as has been observed by others [20,21]. Figure 15 shows instantaneous contours of radial vorticity at the same operating point. The vortex filaments of the tip leakage vortex, which have no radial component at the exit of the tip gap, deform to produce a series of islands of positive and negative radial vorticity which convects across the passage. Low pressure regions associated with these structures were measured by Young et al. [22] on the casing of the large tip gap portion of their axial compressor with eccentric clearance.

*At Stall.* Figure 16 shows simulated casing static pressure traces as the E<sup>3</sup> rotor with tip clearance is brought into stall. When compared with the pressure traces from the two-dimensional and

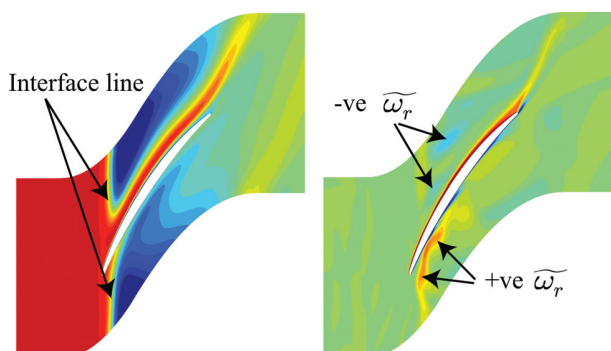


**Fig. 15 Circumferential interface line shown by time-averaged entropy (left); unsteady tip leakage flow shown by instantaneous radial vorticity (right). E<sup>3</sup> rotor with tip clearance, last stable operating point before stall, 95% span.**

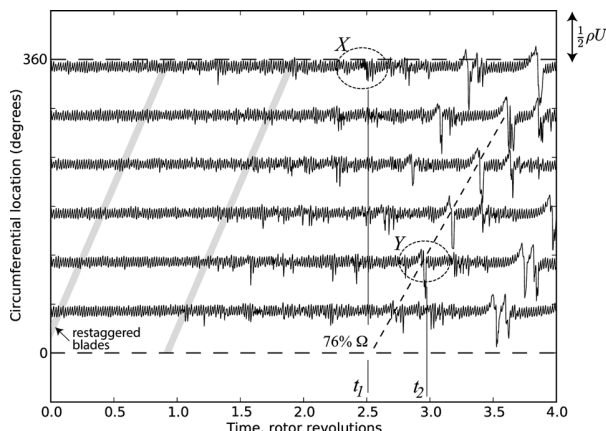


**Fig. 16 Spike stall inception in  $E^3$  rotor computation, with tip clearance**

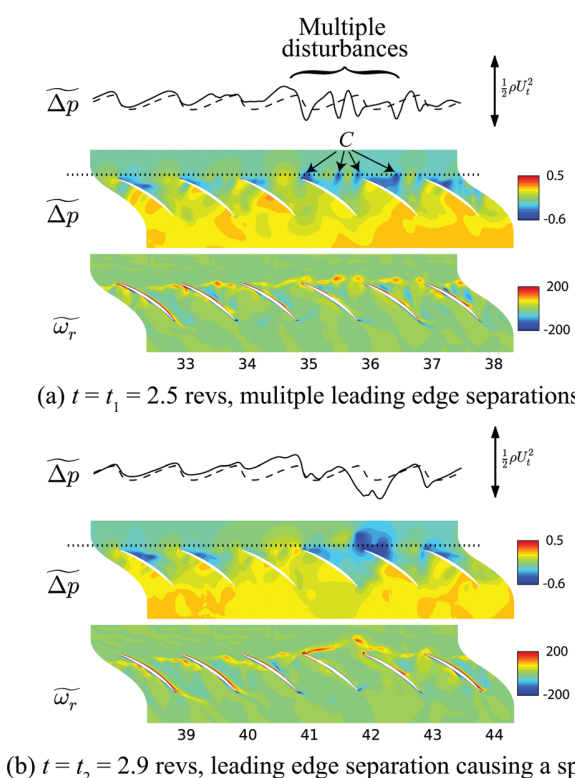


**Fig. 17 Spike formation in  $E^3$  rotor, with clearance, 95% span**

zero clearance cases, two points are apparent. First, there are many disturbances to the regular blade passing signal (particularly narrow low pressure troughs) prior to the final emergence of a spike. Second, the circumferential location of the emergence of spikes is not determined by the restaggered blades and, linked to this, more than one spike is seen. The cause of both of these points will be shown to be the tip clearance flow and, specifically, the unsteadiness of the tip clearance flow.

Figure 17(a) shows a disturbance that later becomes a spike (zone "X" in Fig. 16). In contrast to the two-dimensional and zero clearance cases, no separations are visible on the rear suction surfaces. Instead, it is the tip clearance flow that provides the incidence necessary for leading edge separation. When the tip clearance flow from one blade reaches the leading edge of the next, the incidence is very high (the flow is essentially tangential) and a leading edge separation results. However, because the

clearance flow is itself unsteady, immediately prior to spike stall the fluctuating incidence causes intermittent leading edge separations that do not persist long enough to shed sufficient vorticity to convect to the next blade and trigger a new separation—this is the cause of the multiple disturbances seen in Fig. 16. In addition, if these perturbations in incidence are more than 1 deg in amplitude, the restaggered blades will not provide a trigger for the emergence of a spike. In Fig. 17(a), several vortices have formed from leading edge separations on blades 36 and 37 (labeled "C"). It is not easy to discern from the snapshot shown in Fig. 17(a), but the pressure traces in Fig. 16 indicate that these separations are the early signs of a "successful" spike.

Although the initial stages of spike formation differ for the  $E^3$  case with clearance compared to the preceding two-dimensional and zero clearance cases, the structure and propagation of the spike, Fig. 17(b), are the same. Leading edge separation causes the shedding of vorticity which convects to, and in front of, the adjacent blade where it triggers a new leading edge separation.

The computations of the  $E^3$  rotor with tip gap show that leading edge separation is again responsible for the spike. The cause of the high incidence that leads to this separation is not, however, a growing corner separation but, instead, the tip leakage flow from the adjacent blade. Prior to stall, the unsteadiness of this tip leakage flow causes multiple transient leading edge separations that do not survive (i.e., do not convect in front of the adjacent blades) to form a spike.

**Summary of  $E^3$  Calculations.** All three cases of the  $E^3$  geometry exhibit the same mechanism of spike formation and propagation. In each case, flow separation from the leading edge results in shed radial vorticity which convects to the leading edge of the adjacent blade, triggering a new separation. The principal difference between the simulations is the cause of the incidence that precipitates the leading edge separation. For the two-dimensional and zero clearance cases, the incidence is caused by the blockage from rear suction surface or corner separations. For the case with tip clearance, the incidence is caused by the impingement of the tip leakage flow from the adjacent blade. It is plausible that a rotor with a weaker tip clearance flow (e.g., due to a smaller tip gap) may exhibit corner separations and behave in a similar manner to the zero clearance case. Whatever the particular circumstances that promote high incidence in a given compressor, separation from the leading edge is seen to be the common factor in the structure and propagation of the spike.

### Cambridge Low Speed Compressor

To provide experimental verification of the structures and mechanisms discerned from the  $E^3$  computations, a series of tests were performed on a low speed single-stage compressor at the University of Cambridge. Details of the machine are given by Young et al. [22] and are summarized in Table 2.

The compressor was run with a tip clearance of 1.4% chord. An axial array of five pressure transducers, covering a region from  $-0.4 \leq x/c_x \leq +0.4$  was installed at one circumferential location. Eight additional sensors were placed around the annulus to track stall development. To compare with the experimental data, computations were run on the stage ( $132 \times 10^6$  nodes for the full annulus domain) using the procedure described in the Appendix.

**Table 2 Design parameters for the Cambridge compressor**

Design flow coefficient $V_s/U_t$	0.44
Design stage pressure rise coefficient $\Delta p_0/0.5\rho U_t^2$	0.44
Hub to tip radius ratio $r_h/r_t$	0.75
Tip diameter	488 mm
Number of rotor blades	58
Rotational speed	2980 rpm

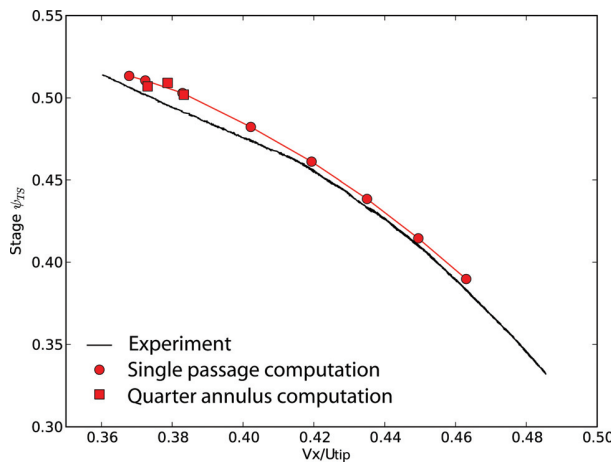
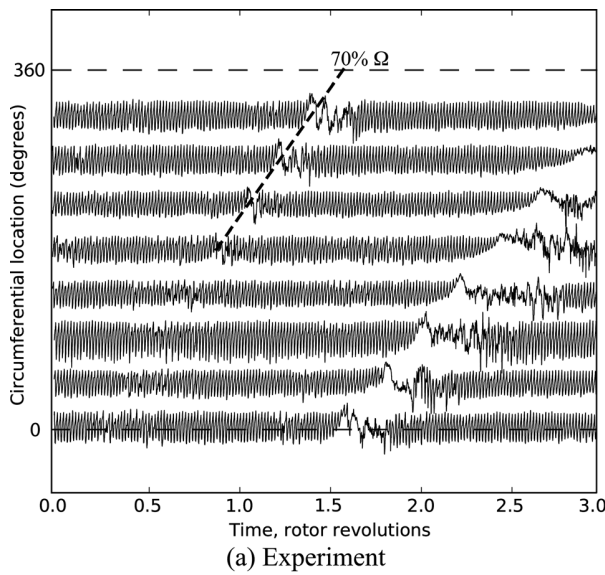
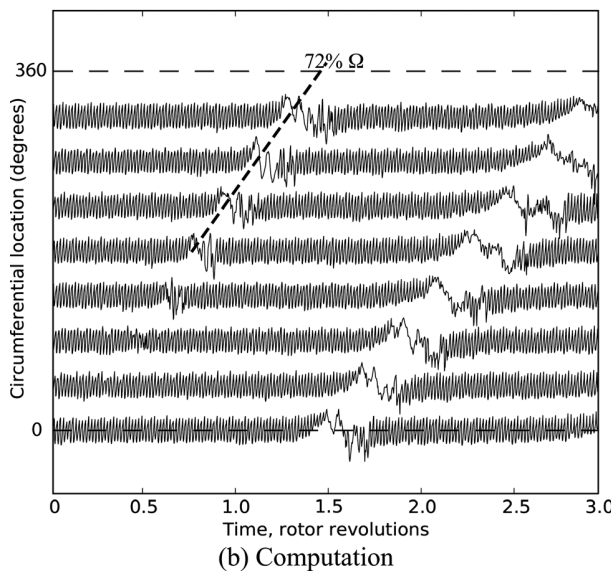


**Fig. 18 Measured and computed total-to-static pressure rise characteristics for the Cambridge compressor**



(a) Experiment



(b) Computation

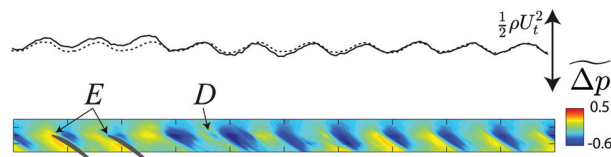
**Fig. 19 Measured and computed casing static pressure traces at the leading edge plane for the Cambridge compressor**

Figure 18 shows measured and calculated total-to-static pressure rise characteristics. As for the  $E^3$  characteristics, Fig. 7, the machine stalls on a negative slope and the quarter-circumference (87 deg in this case) sector computations stall at a higher flow coefficient than those for the single passage. The overall shape of the computed characteristic agrees well with the experiment with the flow coefficient at stall from the simulations 0.01 higher than the measured value.

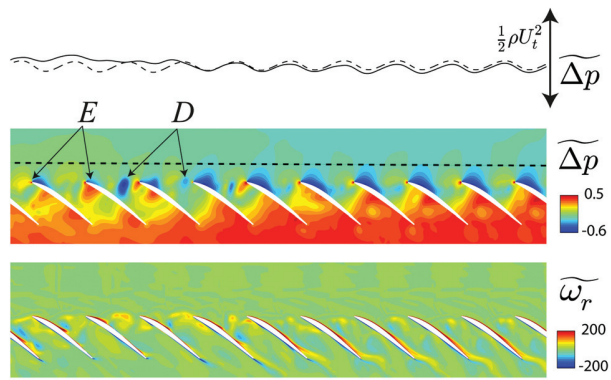
Traces recorded by eight equally spaced casing pressure transducers at the rotor leading edge plane during a stall inception event are shown in Fig. 19(a); equivalent results from a full annulus computation are presented in Fig. 19(b). The close qualitative agreement between the measurement and simulation is encouraging with the spike having a propagation speed, growth rate, and structure (as indicated by the waveform within the stall cell) that are all reproduced well in the computation.

Figure 20 depicts the early stages of spike development ( $t = 0.39$  revs in the computation). Note that the experiments show data from ten blades as they move past the stationary pressure transducers, whereas the CFD is an instantaneous view of ten blades. The computations show that the same mechanism observed in the  $E^3$  simulations is responsible for the formation of the spike: leading edge separation initiated by high incidence caused by the tip leakage flow. The intermittent leading edge separation seen in the  $E^3$  simulations with tip clearance is present in the Cambridge compressor, but the small spatial extent of the vortices (labeled "D") make them hard to discern in the measurements. The reduced blade loading caused by the flow separating from the leading edges of blades labeled "E" is apparent.

At the later time depicted in Fig. 21 ( $t = 0.55$  revs in the computation), the experiments and computations show a spike. A large low pressure region associated with a leading edge separation is seen at "F." The location of this region, including the low pressure zone further aft in the preceding blade passage, is well-reproduced by the computations. The measurements and simulations also show a series of vortices, labeled "G," in the preceding passages



(a) Experimental data: casing  $\widetilde{\Delta p}$ ,  $-0.4 < x/c_x < +0.4$



(b) CFD: traces of  $\widetilde{\Delta p}$  at  $x/c_x = -0.4$ , contours of  $\widetilde{\Delta p}$  and  $\widetilde{\omega}_r$  at 95% span

**Fig. 20 Earliest detection of leading edge separations in the Cambridge compressor ( $t = 0.39$  revs in the computation)**

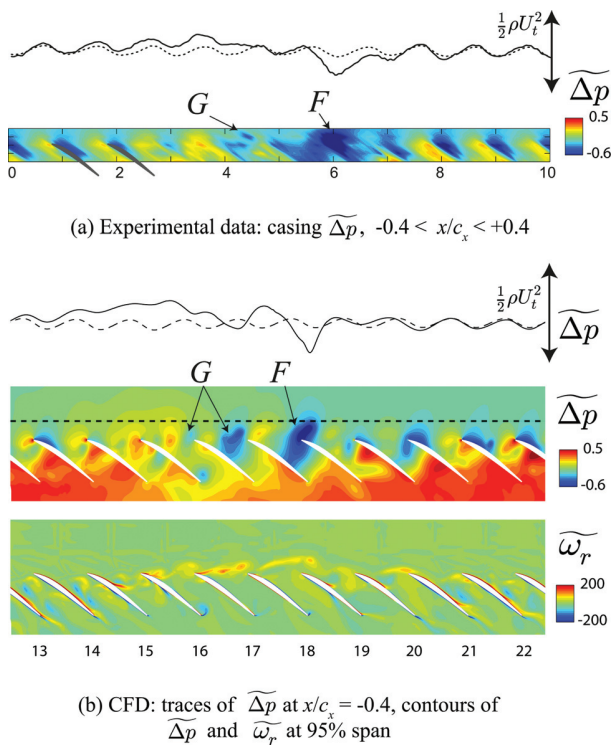


**Fig. 21 Spike caused by leading edge separations in the Cambridge compressor ( $t = 0.55$  revs in the computation)**

(similar vortices are indicated by the detailed casing pressure measurements, at stall inception of a different compressor, reported by Weichert and Day [5]). The trajectory of these vortices indicates that blades 16, 17, and 18 (in the computation) are separated at the leading edge with the associated blockage responsible for the rise on the upstream pressure trace.

The level of agreement between the experiments and computations in terms of overall pressure-rise characteristic, pressure traces upstream of the rotor, and detailed casing flow field data provides strong corroborating evidence for the structures and propagation mechanism of spike-type stall inception seen in the E<sup>3</sup> computations.

## Summary and Conclusions

### Overall Findings

- (1) Numerical simulations and experimental measurements have been used to explain the origins, structure, and propagation mechanism of spike-type disturbances in rotating stall inception. The general features of spike formation are found to be similar in two-dimensional cascades, axial compressor stages with rotor tip clearance and with rotor tip shrouds, and vaned diffusers in centrifugal compressors. In all these geometries, spikes originate from flow separation near the blade leading edge on the suction side, which results in vortex formation and propagation around the annulus.
- (2) The description of spike behavior given here aligns with early ideas put forward by Emmons et al. [14], adding depth and quantitative information to his incidence based mechanism, and by Inoue et al. [10], who initially suggested the involvement of vortex structures in cell formation. The results in the paper show that the description proposed is consistent with both the numerical simulations and the experiments for compressors with a range of differing blade parameters.

### Specific Findings

- (1) Spike-type stall inception involves localized disturbances, of blade passage scale, which propagate from blade to blade around the annulus. The origins of a spike involve radial vorticity, which is shed when flow separates from the leading edge of a blade and then rolls up into a discrete vortex of subpassage proportions. The vortex convects circumferentially toward, and then in front of, the leading edge of the next blade, which experiences increased incidence and then separation and the formation of a new vortex. The pattern of separation, vortex formation, translation, new blade flow separation and renewed vortex formation, explains the structure and propagation mechanism of the spike.
- (2) During stall onset, flow separation causes blockage and a rise in static pressure upstream of the blade row with circumferential extent of a few blade pitches. This localized increase in pressure is observed as a sharp upward peak in measurement data and is responsible for the classification of this type of disturbance as a “spike.”
- (3) The shed vortex that accompanies the leading edge separation gives rise to a region of low static pressure on the compressor casing. The resulting pattern of a region of high pressure adjacent to a region of low pressure gives rise to the typical up-down signature of a maturing spike seen in pressure signal recorded upstream of the rotor.
- (4) The experimental and computational results agree and they suggest that spike formation is not dependent on tip leakage flow. More precisely, the vortex described above is not associated with the tip leakage flow in that the same general features are observed in blade rows with and without tip clearance. In cases where tip clearance is present, as in a conventional axial compressor, the leakage flow contributes to high incidence at the rotor tips, but the leakage flow itself is not a requirement for flow separation and spike formation.
- (5) The fluid dynamic processes that give rise to the incidence that creates the initial leading edge separation depend on the details of the blades being used. For a two-dimensional cascade, the separation process begins at the trailing edge of the blade and works its way toward the leading edge. In a three-dimensional case without tip clearance, corner separation can play a part in triggering separation at the leading edge. In a conventional blade row with tip clearance, leakage flow can sometimes exacerbate leading edge incidence. In all cases, however, regardless of the precise cause of increased incidence, spike development is due to leading edge flow separation and vortex formation.

### Acknowledgment

The authors gratefully acknowledge the contributions made by several individuals during many discussions on the topics described in this paper, including those provided by C. Freeman and S. A. Weichert of the Whittle Laboratory, N. A. Cumpsty of Imperial College, and J. J. Adamczyk. The authors would also like to thank S. Aoki, S. Uchida and E. Ito of MHI for their support during the project; J. J. Bolger of Rolls-Royce for supplying the geometry of the Cambridge Low Speed Compressor and for supporting the associated experimental program; and M. Brand and A. Kottapalli for taking the data on the MIT shrouded compressor.

### Nomenclature

- $c_x$  = axial chord
- $p$  = pressure
- $p_{01}$  = rotor inlet stagnation pressure
- $r_t$  = tip radius

$$\begin{aligned}
t &= \text{time} \\
U_t &= \text{tip speed} \\
x &= \text{axial distance, measured from the leading edge} \\
\Delta p &= \text{pressure coefficient} = (p - p_{01}) / (\frac{1}{2} \rho U_t^2) \\
\rho &= \text{density} \\
\tau &= \text{blade passing period} \\
\psi_{TS} &= \text{total-to-static pressure rise coefficient} = (p_{exit} - p_{01}) / (\frac{1}{2} \rho U_t^2) \\
\Omega &= \text{rotor angular velocity} \\
\tilde{\omega}_r &= \text{nondimensional radial vorticity} = \omega_r / (U_t / r_t)
\end{aligned}$$

## Appendix: Details of the Computational Approach

All the computations presented in this paper were performed using Turbostream [11]. The code is a structured multiblock RANS solver that was developed using the method employed in the Denton code, TBLOCK [23]. The approach is finite-volume time-marching, second order in space, with three levels of multi-grid and a single step explicit time integration scheme. All simulations presented here used the Spalart–Allmaras turbulence model with adaptive wall functions and had fully turbulent boundary layers. All the runs were second order accurate in time using Jameson’s dual timestepping technique, with 72 physical time steps per blade passing period.

The principal feature of Turbostream is its speed. As well as running on conventional central processing units (CPU), the code is also optimized to run on clusters of GPUs. Turbostream runs 10–20 times faster on one GPU as compared to all cores of a contemporaneous CPU. This allowed an operating point of the quarter annulus ( $\approx 20 \times 10^5$  node for the  $E^3$  domain) calculations to be completed in 1 day on 32 GPUs.

The grids were generated using a Mitsubishi Heavy Industries in-house code that produced elliptically smoothed blade row meshes with H–O–H topology. Tip gaps were solved with two additional blocks (O–H topology) with 11 points in the gap. All blades were meshed with  $293 \times 37 \times 74$  points in the O-mesh, with approximately 30 points around the leading edge, and typical  $y^+$  values were below 5 on the blade surfaces. The computational domain extended 1.5 tip radii upstream and downstream of the blade rows. This gave an axial distance of approximately one quarter of a circumference between the compressor and the planes at which inlet or outlet boundary conditions were imposed. To reduce the mesh count required, the pitchwise node count per passage was reduced from 57 at the blade row, to 15 at the domain boundaries in three stages.

At the inlet of the domain, the total pressure and total temperature were specified as uniform. However, a portion at the start of the inlet duct was set to have zero skin friction in order to control the inlet endwall boundary layer thickness. The boundary layer thickness was matched to measurement data for the Cambridge compressor. At the exit of the domain, a convergent nozzle was employed to provide the compressor with a back-pressure that changes with mass flow rather than a fixed pressure boundary condition [24]. The nozzle was not choked, so that altering the pressure downstream of the nozzle (specified to be uniform) caused the compressor operating point to change and the pressure upstream of the nozzle to vary according to the matching of the compressor characteristic and the characteristic of the nozzle.

Each operating point was run for five flow-through times (from domain inlet to exit); this was of the order of 4 rotor revolutions. Over the first rotor revolution, the back pressure at the exit of the nozzle was increased linearly with time and the flow coefficient

typically reduced by 0.01. This procedure was done first with a single passage domain to obtain the approximate stall point, then with a quarter annulus domain, and finally with a full annulus.

Postprocessing is a formidable task with unsteady datasets of order  $10^8$  nodes. The approach taken was similar to that of the experimentalist. Several measurement planes were output 12 times per rotor passing period, e.g., a selection of blade-to-blade planes, rotor blade surface, and rotor exit planes. From these, a particular range of times was identified for deeper analysis and the operating point was then rerun to obtain this data.

## References

- [1] Camp, T., and Day, I., 1998, "A Study of Spike and Modal Stall Phenomena in a Low-Speed Axial Compressor," *ASME J. Turbomach.*, **120**(3), pp. 393–401.
- [2] Garnier, V., Epstein, A., and Greitzer, E., 1991, "Rotating Waves as a Stall Inception Indication in Axial Compressors," *ASME J. Turbomach.*, **113**(2), pp. 290–301.
- [3] Lin, F., Chen, J., and Meilin, L., 2004, "Wavelet Analysis of Rotor-Tip Disturbances in an Axial-Flow Compressor," *AIAA J. Propul. Power*, **20**(2), pp. 319–334.
- [4] Deppe, A., Saathoff, H., and Stark, U., 2005, "Spike-Type Stall Inception in Axial-Flow Compressors," 6th European Conference on Turbomachinery, Lille, France, Mar. 7–11, pp. 178–188.
- [5] Weichert, S., and Day, I., 2014, "Detailed Measurements of Spike Formation in an Axial Compressor," *ASME J. Turbomach.*, **136**(5), p. 051006.
- [6] Brand, M., Kottapalli, A., and Spakovszky, Z., 2011, The Dependence of Spike-Type Stall Inception on Blade-Tip Leakage Flow in Axial Compressors," 16.62X Final Report, Experimental Projects Course, Department of Aeronautics and Astronautics, MIT, Cambridge, MA.
- [7] Spakovszky, Z., and Roduner, C., 2009, "Spike and Modal Stall Inception in an Advanced Turbocharger Centrifugal Compressor," *ASME J. Turbomach.*, **131**(3), p. 031012.
- [8] Everitt, J., and Spakovszky, Z., 2011, "An Investigation of Stall Inception in Centrifugal Compressor Vaned Diffusers," *ASME Paper No. GT2011-46332*.
- [9] Vo, H., Tan, C., and Greitzer, E., 2008, "Criteria for Spike Initiated Rotating Stall," *ASME J. Turbomach.*, **130**(1), p. 011023.
- [10] Inoue, M., Kuromaru, M., Tanino, T., and Furukawa, M., 2000, "Propagation of Multiple Short-Length-Scale Stall Cells in an Axial Compressor Rotor," *ASME J. Turbomach.*, **122**(1), pp. 45–54.
- [11] Brandvik, T., and Pullan, G., 2011, "An Accelerated 3D Navier–Stokes Solver for Flows in Turbomachines," *ASME J. Turbomach.*, **133**(2), p. 021025.
- [12] Pullan, G., Denton, J., and Curtis, E., 2006, "Improving the Performance of a Turbine With Low Aspect Ratio Stators by Aft-Loading," *ASME J. Turbomach.*, **128**(3), pp. 492–499.
- [13] Wisler, D. C., 1977, "Core Compressor Exit Stage Study: Vol. 1—Blading Design," NASA Lewis Research Center, Cleveland, OH, Report No. NASA CR-135391.
- [14] Emmons, H., Pearson, C., and Grant, H., 1955, "Compressor Surge and Stall Propagation," *Trans. ASME*, **79**(4), pp. 455–469.
- [15] Jeong, J., and Hussain, F., 1995, "On the Identification of a Vortex," *J. Fluid Mech.*, **285**, pp. 69–94.
- [16] Inoue, M., Kuromaru, M., Tanino, T., Yoshida, S., and Furukawa, M., 2001, "Comparative Studies on Short and Long Length-Scale Stall Cell Propagating in Axial Compressor Rotor," *ASME J. Turbomach.*, **123**(1), pp. 24–30.
- [17] Inoue, M., Kuromaru, M., Yoshida, S., and Furukawa, M., 2002, "Short and Long Length-Scale Disturbances Leading to Rotating Stall in an Axial Compressor Stage With Different Stator/Rotor Gaps," *ASME J. Turbomach.*, **124**(3), pp. 376–384.
- [18] Inoue, M., Kuromaru, M., Yoshida, S., Minami, T., Yamada, K., and Furukawa, M., 2004, "Effect of Tip Clearance on Stall Evolution Process in a Low-Speed Axial Compressor Stage," *ASME Paper No. GT2004-53354*.
- [19] Yamada, K., Kikuta, H., Iwakiri, K., Furukawa, M., and Gunjishima, S., 2013, "An Explanation for Flow Features of Spike-Type Stall Inception in an Axial Compressor Rotor," *ASME J. Turbomach.*, **135**(2), p. 021023.
- [20] Mailach, R., Lehmann, I., and Vogeler, K., 2001, "Rotating Instabilities in an Axial Compressor Originating From the Fluctuating Blade Tip Vortex," *ASME J. Turbomach.*, **123**(3), pp. 453–460.
- [21] März, J., Hah, C., and Neise, W., 2002, "An Experimental and Numerical Investigation Into the Mechanisms of Rotating Instability," *ASME J. Turbomach.*, **124**(3), p. 375.
- [22] Young, A., Day, I., and Pullan, G., 2012, "Stall Warning by Blade Pressure Signature Analysis," *ASME J. Turbomach.*, **135**(1), p. 011033.
- [23] Rosic, B., Denton, J., and Pullan, G., 2006, "The Importance of Shroud Leakage Modeling in Multistage Turbine Flow Calculations," *ASME J. Turbomach.*, **128**(4), pp. 699–707.
- [24] Vahdati, M., Sayma, A., Freeman, C., and Imregun, M., 2005, "On the Use of Atmospheric Boundary Conditions for Axial-Flow Compressor Stall Simulations," *ASME J. Turbomach.*, **127**(2), pp. 349–351.